Catalysis Today 141 (2009) 109–114

Contents lists available at ScienceDirect

Catalysis Today

journal homepage: www.elsevier.com/locate/cattod

Highly dispersed ceria and ceria–zirconia nanocomposites over silica surface for catalytic applications

Benjaram M. Reddy *, Pranjal Saikia, Pankaj Bharali, Lakshmi Katta, Gode Thrimurthulu

Inorganic and Physical Chemistry Division, Indian Institute of Chemical Technology, Uppal Road, Hyderabad 500607, India

ARTICLE INFO

Article history:
Available online 24 June 2008

Keywords:
Ceria
CeO_2/SiO_2
$CeO_2–ZrO_2/SiO_2$
Structural characterization
Oxygen storage capacity (OSC)

ABSTRACT

Silica-supported CeO_2 and $CeO_2–ZrO_2$ nanocomposite oxides were synthesized by a novel deposition–precipitation method and subjected to thermal treatments at 773–1073 K to study their sintering behavior and oxygen storage/release capacity (OSC). The prepared catalysts were characterized using thermogravimetry, BET surface area, X-ray diffraction, Raman spectroscopy, X-ray photoelectron spectroscopy, high-resolution transmission electron microscopy and other techniques. BET measurements indicate that $CeO_2–ZrO_2/SiO_2$ (CZS) samples possess more specific surface area and substantial resistance towards thermal sintering relative to CeO_2/SiO_2 (CS) samples. XRD profiles reveal only the broad diffraction lines due to CeO_2 in the case of CS while CZS discloses $Ce_{0.75}Zr_{0.25}O_2$, $Ce_{0.6}Zr_{0.4}O_2$ and $Ce_{0.5}Zr_{0.5}O_2$ phases depending on the treatment temperature. Raman measurements of both series of samples indicate the presence of oxygen vacancies, lattice defects and displacement of oxygen ions from their ideal lattice positions. XPS studies indicate the presence of cerium at the surface in both 4+ and 3+ oxidation states. The HREM results reveal well dispersed CeO_2 (~3–4 nm) and Ce–Zr oxide particles (~5 nm) over the amorphous SiO_2 matrix in the case of CS and CZS samples, respectively. There was no significant increase in the size of the dispersed nano-oxides even after calcination at 1073 K. Both the samples exhibit reasonably high OSC values.

1. Introduction

Ceria and its composite oxides, particularly ceria–zirconia in different stoichiometries, regardless of unsupported or supported forms, have received tremendous attention recently owing to their crucial role in several catalytic applications including three-way catalysis for automotive exhaust gas purification [1–5], cracking of heavy oils [6], cracking and reforming of methane with CO_2 and/or with steam [7,8], water-gas shift reaction [9–11] and so on. The wide applicability of ceria is due to its unique acid–base and redox properties. It is well-known that ceria can affect (i) the thermal and structural stability of the catalyst carriers [12], (ii) the dispersion of supported metals [13], (iii) the facile oxidation and reduction of noble metals [14], (iv) oxygen storage and release characteristics of the composites [15] and (v) the decrease of carbonaceous formation on the catalyst surfaces [8]. The high oxygen storage/release capacity (OSC) is a result of high reducibility of Ce^{4+}, which is a consequence of high mobility of O^{2-} ions inside the ceria lattice [6]. Relative to ceria alone, ceria–zirconia mixed oxides are known to bear a high thermal resistance and increased OSC. Incorporation of zirconium into ceria leads to structural modification of the cubic fluorite structure of ceria that result in the decrease of the cell volume and activation energy for oxide ion diffusion [3].

Highly dispersed, monomolecular layers of active oxides deposited on the surface of an inert support have been intensively studied for many years, mainly due to their catalytic applications [16]. Currently, ceria-based systems are usually supported on transition aluminas, with the aim of achieving better dispersion of the active phase and improvement of oxygen exchange rate. Silica is another most widely available supports with excellent chemical resistance, thermal stability and high specific surface area, which can enhance dispersion and thereby the catalytic activity of the dispersed active oxides. In the present investigation, silica-supported ceria and ceria–zirconia nanocomposite oxides were synthesized by a novel deposition–precipitation method employing colloidal silica and subjected to thermal treatments to understand the dispersion and temperature stability of these materials. These effects were systematically investigated using thermogravimetry analysis (TGA), BET surface area, X-ray diffraction (XRD), Raman spectroscopy, high-resolution transmission electron microscopy (HREM), X-ray photoelectron spectroscopy (XPS) and other techniques. The oxygen storage/release capacity

* Corresponding author. Tel.: +91 40 2716 0123; fax: +91 40 2716 0921.
E-mail addresses: bmreddy@iict.res.in, mreddyb@yahoo.com (B.M. Reddy).

0920-5861/$ – see front matter © 2008 Elsevier B.V. All rights reserved.
doi:10.1016/j.cattod.2008.05.008

was determined by a thermogravimetry method to evaluate the quality of these materials for catalytic applications.

2. Experimental

2.1. Catalyst preparation

The CeO_2/SiO_2 (CS) (1:1 mole ratio based on oxides) and CeO_2–ZrO_2/SiO_2 (CZS) (1:1:2 mole ratio based on oxides) samples were prepared by a deposition precipitation method from ultra high dilute aqueous solutions of ammonium cerium(IV) nitrate (Loba Chemie, GR grade), zirconium(IV) nitrate (Fluka, AR grade) and colloidal silica (Ludox 40 wt.%, Aldrich, AR grade). In a typical procedure, requisite quantities of nitrate salts were dissolved separately in deionized water and mixed together. Required quantity of colloidal silica was added to the aforementioned individual or mixture solutions. Dilute aqueous ammonia was added drop-wise with vigorous stirring until the precipitation was complete (pH ~ 8.5). The resulting product was filtered off, washed several times with deionized water, oven dried at 383 K for 12 h and calcined at 773 K for 5 h in air atmosphere. Portions of the calcined samples were once again heated at 1073 K for 5 h.

2.2. Catalyst characterization

The TG–DTA curves were obtained on a Mettler Toledo TG-SDTA apparatus. The heating rate was 10 K/min. The BET surface areas were determined by N_2 physisorption at liquid N_2 temperature on a Micromeritics Gemini 2360 Instrument. XRD patterns were recorded on a Siemens D-5005 diffractometer using nickel-filtered Cu Kα (0.15418 nm) radiation source. Crystalline phases were identified by comparison with the reference data from ICDD files. The average crystallite sizes were estimated with the help of Scherrer equation using the XRD data of all prominent lines [17]. The cell *a* parameter values were calculated by a standard cubic indexation method using the intensity of ceria base peak (1 1 1) [18]. The Raman spectra were recorded on a DILOR XY spectrometer equipped with a liquid N_2 cooled CCD detector at ambient temperature and pressure. The emission line at 514.5 nm from an Ar^+ ion laser (Spectra Physics) was focused on the sample under microscope and the wavenumbers obtained from spectra are accurate to within 2 cm^{-1}. The XPS measurements were performed on a Shimadzu (ESCA 3400) spectrometer by using Mg Kα (1253.6 eV) radiation as the excitation source at ambient temperature and pressures typically in the order of less than 10^{-6} Pa. Charging of catalyst samples was corrected by setting the binding energy of the adventitious carbon (C 1s) at 284.6 eV [19,20]. The TEM-HREM images were recorded on Philips CM200 and JEOL 2000EX electron microscopes with 0.23 and 0.21 nm point-to-point resolutions, respectively. For these studies, a suspension of the sample in ethanol was placed in an ultrasound bath and then a drop of it was supported on a holey carbon grid.

The OSC of the sample was measured in terms oxygen release characteristics in the temperature range 573–1073 K. The change in weight of the sample was monitored by thermogravimetry under cyclic heat treatments in flowing nitrogen and dry air. The heat cycle consisted of heating the sample to 1073 K, cooling to 423 K, and again heating to 1073 K. All heating and cooling rates were at 5 K/min. The weight loss of the sample during the second stage of heat treatment was used to measure the oxygen release property [21]. A commercial Netzsch (Luxx, STA, 409 PC, Germany) TG–DTA analyzer was employed for this purpose.

3. Results and discussion

The CS and CZS composite oxides were subjected to TG–DTA analysis before calcination, which revealed one major and two minor weight loss peaks. The major low temperature peak in the range 309–463 K arises primarily due to loss of non-dissociative adsorbed water as well as water held on the surface by hydrogen bonding. The minor weight loss peak in the 550–584 K range was due to loss of water held in the micropores of the mixed oxide gel. A further loss of water occurred around 633–723 K due to dehydroxylation of the surface. In the case of CS sample, the loss of weight from ambient to 470 K was about 10% and from 470 to 723 K it was 5%. However, the weight loss between 723 and 1073 K was only about 1%. The weight loss, in the case of CZS sample, from ambient to 520 K was about 12% and from 520 to 840 K it was 4.2%. However, the weight loss between 840 and 1073 K was only about 0.3%. It indicates that over the temperature range between 840 and 1073 K, the CZS mixed oxide is quite stable in terms of chemical and phase composition. The N_2 BET surface areas of various samples are presented in Table 1. As can be noted, the surface area of CZS is much higher compared to that of CS when calcined at 773 K. At higher calcination temperature both series of samples lose the surface area due to sintering and better crystallization of the mixed oxide phases.

The XRD patterns of CS and CZS samples calcined at 773 and 1073 K are shown in Fig. 1. The 773 K calcined samples exhibit relatively poor crystallinity. Only the broad diffraction lines due to CeO_2 (PDF–ICDD 34-0394, lattice parameter 5.41 Å) are visible in the case of CS sample. With increasing calcination temperature from 773 to 1073 K, an increase in the intensity of the peaks due to better crystallization of cerium oxide is noted. The CZS sample calcined at 773 K revealed the presence of $Ce_{0.75}Zr_{0.25}O_2$ (PDF–ICDD 28-0271, lattice parameter 5.35 Å) phase. An increase in the intensity of the lines accompanied by a slight shift in the peak positions due to the formation of $Ce_{0.6}Zr_{0.4}O_2$ (PDF–ICDD 38-1439, lattice parameter 5.31 Å) and $Ce_{0.5}Zr_{0.5}O_2$ (PDF–ICDD 38-1436, lattice parameter 5.30 Å) phases along with $Ce_{0.75}Zr_{0.25}O_2$ phase are noted at 1073 K. The formation of new phases is mainly due to a progressive increase of Zr^{4+} ion content in the ceria unit cell, which is also clearly reflected by a decrease in the lattice parameter with increasing calcination temperature (Table 1). As Zr^{4+} bears ionic radius (0.84 Å) smaller than Ce^{4+} (0.97 Å), lattice contraction

Table 1
BET surface area, average crystallite size and lattice parameter measurements of CeO_2/SiO_2 and CeO_2–ZrO_2/SiO_2 samples calcined at different temperature

Sample	Calcination temperature (K)	BET SA ($m^2\,g^{-1}$)	Crystallite size[a] (nm)	Lattice parameter (Å)	Weight loss[b] (%)	OSC (μmol O_2/g ceria)
CeO_2/SiO_2	773	147	3.2	5.41	0.39	121.8
	1073	54	6.0	5.40	0.35	109.3
CeO_2–ZrO_2/SiO_2	773	172	3.1	5.35	0.65	490.5 (286)[c]
	1073	112	3.7	5.26	0.62	451.2 (263)[c]

[a] CeO_2 and $Ce_{0.75}Zr_{0.25}O_2$ in CeO_2/SiO_2 and CeO_2–ZrO_2/SiO_2 samples, respectively.
[b] Weight loss in second heating cycle.
[c] μmoles of O_2/g of ceria–zirconia (in parenthesis).

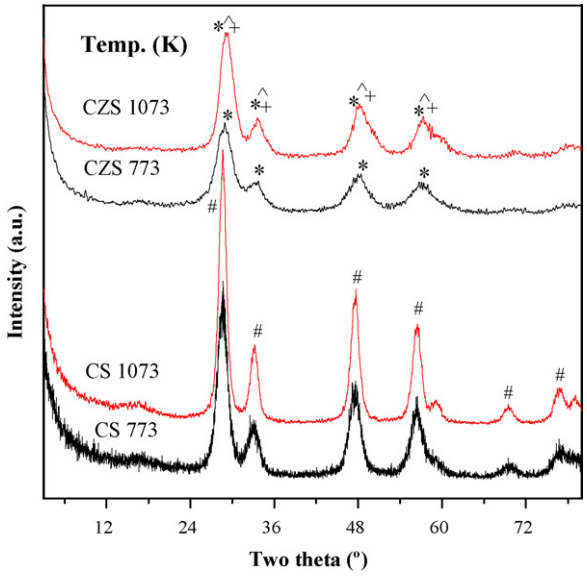

Fig. 1. XRD patterns of CeO_2/SiO_2 (CS) and CeO_2–ZrO_2/SiO_2 (CZS) samples calcined at 773 and 1073 K. (#) Lines due to CeO_2, (*) lines due to $Ce_{0.75}Zr_{0.25}O_2$, (^) lines due to $Ce_{0.6}Zr_{0.4}O_2$ and (+) lines due to $Ce_{0.5}Zr_{0.5}O_2$.

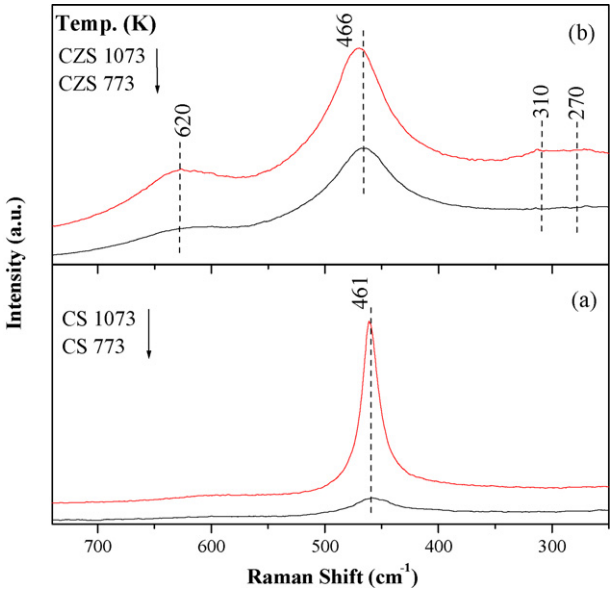

Fig. 2. Raman spectra of CeO_2/SiO_2 (CS) and CeO_2–ZrO_2/SiO_2 (CZS) samples calcined at 773 and 1073 K.

occurs when more zirconium enters the ceria lattice. No significant change in the lattice parameter value is noted in the case of CS sample (5.40 Å). The silica features were not observed from the XRD measurements [22]. It is also known that ceria and silica do not form compounds or mixed phases as observed for ceria–zirconia mixed oxides within 1073 K [10,22]. The crystallite size of CeO_2 and $Ce_{0.75}Zr_{0.25}O_2$ in CS and CZS samples, respectively, estimated from XRD measurements revealed a nominal increase with increasing calcination temperature (Table 1). This signifies the influence of silica support to prevent agglomeration of the oxide particles.

As presented in Fig. 2a, the Raman spectrum of CS sample calcined at 773 K shows a prominent peak at ~457 cm^{-1} and a weak band at ~600 cm^{-1}. The band at around 457 cm^{-1} corresponds to triply degenerate F_{2g} mode and can be viewed as a symmetric breathing mode of oxygen atoms around cerium ions [23]. Only one mode is Raman active for the cubic fluorite structure of ceria (space group *Fm*3*m*) [24]. With increasing calcination temperature from 773 to 1073 K, the band at ~457 cm^{-1} shifted to ~461 cm^{-1}, sharpened and become more symmetrical. This is due to better crystallization of ceria at higher calcination temperature in line with XRD results. The weak band observed at 600 cm^{-1} corresponds to a doubly degenerate LO mode of CeO_2 [25]. In particular, this band has been linked to oxygen vacancies in the CeO_2 lattice [26]. The Raman spectrum of CZS sample (Fig. 2b) calcined at 773 K exhibited a strong band at ~464 cm^{-1} along with a broad hump at ~620 cm^{-1}. The band at ~464 cm^{-1} is due to symmetric O–Ce–O stretching mode as mentioned earlier. According to literature, six Raman active modes ($A_{1g} + 3E_g + 2B_{1g}$) are expected for *t*-ZrO_2 (space group *P*42/*nmc*) but no Raman lines due to ZrO_2 could be observed in the present study [27]. The Raman bands of CZS are broader than CS samples. The broadness and shift of Raman bands in the case of CZS samples could be attributed to the presence of $Ce_xZr_{1-x}O_2$ phases since several factors influence the intensity of Raman bands [28]. It is known from the literature that sintering of samples under high temperature conditions leads to the formation of oxygen vacancies, which perturb the local M–O bond symmetry leading to the relaxation of symmetry selection rules [24]. The appearance of weak bands at ~310 cm^{-1} after calcination at 1073 K can be attributed to displacement of the oxygen atoms from their ideal fluorite lattice positions [29]. Silica did not show any Raman features, as reported in the literature [30]. This gives an impression that silica forms part of the substrate support on which ceria or ceria–zirconia solid solutions are dispersed. It is expected since the method of preparation adopted in the present study could result such a material.

Table 2
Core level binding energy values (eV) for CeO_2/SiO_2 and CeO_2–ZrO_2/SiO_2 samples calcined at 773 and 1073 K

Sample	Calcination temperature (K)	O 1s	Ce 3d	Zr 3d	Si 2p
CeO_2/SiO_2	773	530.1	881.7	–	103.7
	1073	530.2	881.2	–	103.8
CeO_2–ZrO_2/SiO_2	773	530.1	881.4	182.5	102.9
	1073	530.3	881.1	182.4	103.2

The CS and CZS samples were analyzed by XPS technique to verify the elemental oxidation states. The electron binding energies of O 1s, Ce 3d, Zr 3d and Si 2p are presented in Table 2 which agree well with the literature reports [19,20]. As presented in Fig. 3, the O 1s profile is broad and complicated due to the overlapping contribution of oxygen from ceria and silica in the case of the CS and ceria, silica and zirconia in the case of CZS sample, respectively. The binding energy of the most intense O 1s peak (Table 2), in the case of the CS sample, is almost constant with increasing calcination temperature. The observed intense peak at about 530.1 eV belongs to the oxygen atoms that are bound to Ce [19,20]. Compared to CS sample, in the case of CZS sample, a slight shift in the peak maxima is noticed. This indicates some changes in the oxygen environment in the CZS sample which is obvious due to the presence of both ceria and zirconia along with SiO_2. In other words, it hints that structural changes occurred in the ceria lattice. Further, the O 1s binding energy values show a small increase with increase of calcination temperature in this case. The observed shift in the BE values could be attributed to a gradual increase in the zirconium content in the cubic fluorite type ceria lattice. As reported in the literature, the oxygen ions in pure SiO_2 and CeO_2 exhibit intense peaks at 532.7 and 528.6 eV, respectively [31]. It

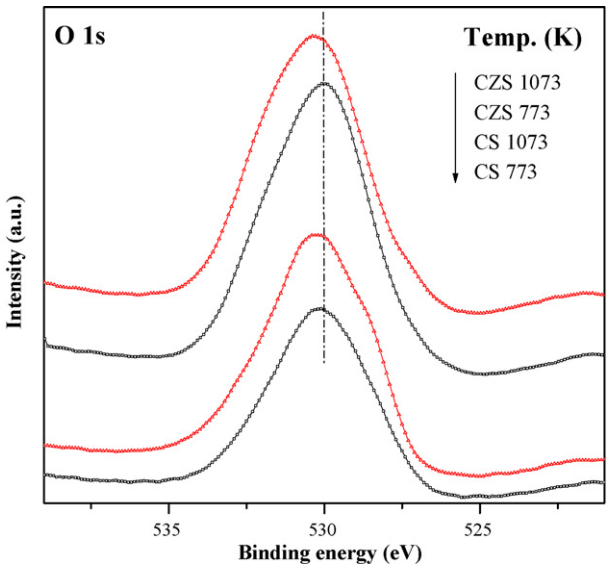

Fig. 3. Core level O 1s XP spectra of CeO_2/SiO_2 (CS) and CeO_2–ZrO_2/SiO_2 (CZS) samples calcined at 773 and 1073 K.

appears that the silica surface has been covered by the dispersed CeO_2 and $Ce_xZr_{1-x}O_2$ oxides.

Fig. 4 shows the Ce 3d photoelectron peaks of the CS and CZS samples calcined at 773 and 1073 K. The binding energy values obtained for Ce 3d peaks (Table 2) were found to be within the range of the values reported in the literature [25,26]. The assignment of Ce 3d photoelectron peaks is not easy due to the complex nature of the spectra arising due to multiple oxidation states and mixing of Ce 4f levels and O 2p states during the photoemission process [19]. The notation of Burroughs et al. could be used to explain the Ce 3d peaks as shown in the figure [32]. The peaks labelled as v correspond to Ce $3d_{5/2}$ contributions and those as labelled u represent the Ce $3d_{3/2}$ contributions. Specifically, the bands u_o and u are due to Ce $3d_{3/2}$ ionization and bands v_0 and v are Ce $3d_{5/2}$ ionizations for Ce^{3+} and Ce^{4+}, respectively. The bands labelled as v′, v″ and v‴, are satellites arising from the $3d_{5/2}$ ionization, while the bands u′, u″ and u‴ represent Ce $3d_{3/2}$ ionization. The XPS spectra of both CS and CZS samples calcined at 773 K exhibit peaks due to the presence of both Ce^{4+} and Ce^{3+}, thus implying that cerium is present at the surface in both 4+ and 3+ oxidation states. With increasing calcination temperature from 773 to 1073 K the relative intensity of u′ and v′ annotated peaks increased, indicating an increase in the surface content of Ce^{3+}. The u‴ peak is the most convenient feature to follow the progressive reduction of ceria, since it does not overlap with others. As the calcination temperature increases the intensity of the u‴ peak decreased indicating the decrease of Ce^{4+} state. However, there lies a certain possibility that the Ce^{3+} has been formed due to the reduction of CeO_2 under the conditions of ultra high vacuum during XPS measurements. Literature reveals that ceria in CZS sample becomes easily reducible due to formation of solid solutions with zirconia [32].

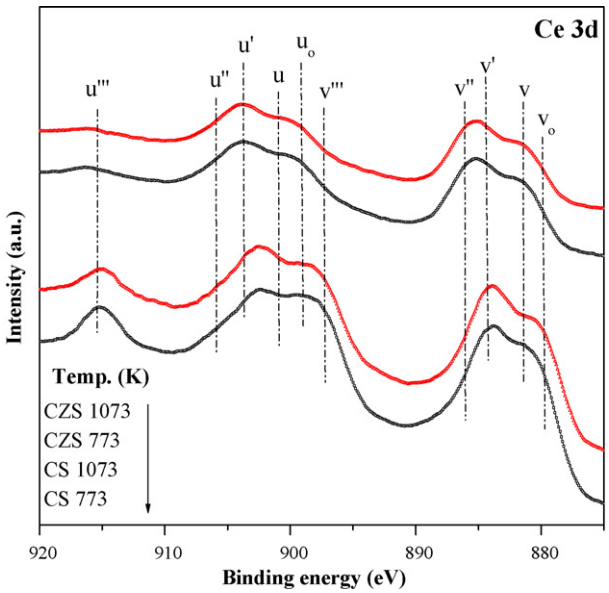

Fig. 4. Core level Ce 3d XP spectra of CeO_2/SiO_2 (CS) and CeO_2–ZrO_2/SiO_2 (CZS) samples calcined at 773 and 1073 K.

As can be envisaged from Table 2, the binding energy of the Si 2p peak ranged between 102.9 and 103.7 eV, which agree well with the values reported in the literature [19,20]. The spectra were poor in intensity with large peak widths indicating that silica is not easily accessible at the surface due to the presence of CeO_2 and $Ce_xZr_{1-x}O_2$ over layer in CS and CZS samples, respectively. Further, no change in the intensity of the Si 2p core level spectra with increasing calcination temperature revealed that no significant redistribution of various components under high temperature treatment has taken place. The presence of oxidized silicon has been abundantly described in the literature, sometimes as CeO_{2-x}/SiO_2 or as an amorphous silicate layer where partial reduction of Ce^{4+} to Ce^{3+} occurs together with partial oxidation of Si [33]. There is no clue regarding the formation of either $CeSiO_4$ or $ZrSiO_4$ that could be identified by the Si 2p binding energy value of 101 eV [34]. The binding energy of the Zr 3d photoelectron peak ranged between 182.4 and 182.5 eV (Table 2) that agrees well with the literature, could be taken as an evidence for the absence of free ZrO_2 for which the binding energy value is expected to be 182.9 eV [19,20].

The TEM image of the CS sample calcined at 773 K is shown in Fig. 5a. A careful inspection of the image revealed the existence of smaller crystals (~3–4 nm) dispersed over an amorphous matrix with different contrasts. For deeper insight, the high-resolution images (HREM) were undertaken to establish the structure of the particles (inset of Fig. 5a). The contrast observed in the experimental image is associated to the face-centered cubic structure (fluorite) of the cerium oxide. Well-crystallized CeO_2 grains mixed with SiO_2 (amorphous matrix) are mainly observed [35]. The digital diffraction pattern (DDP) obtained from the experimental image is also shown as inset in Fig. 5a. The spots labeled 1, 2 and 3 in the DDP correspond to the interplanar spacings of 3.2, 2.7 and 3.1 Å, respectively which correspond to the (1 1 1), (2 0 0) and (1 −1 −1) planes of ceria in cubic fluorite structure. The energy dispersive X-ray microanalysis (EDX) was also performed to get information on the composition of the surface, which revealed the presence of Ce and Si in stoichiometric proportions. Fig. 5b shows a representative TEM image of the CS sample calcined at 1073 K. The presence of ceria nano-crystals dispersed over the amorphous silica is mainly seen from this image. The mean size of the CeO_2 crystals increased from ~3–4 to ~6–10 nm. The HREM image and the corresponding digital diffraction pattern are also shown in Fig. 5b (inset). The ceria crystallites can be discriminated as patches of parallel lattice fringes with a distance of ~3.2 Å corresponding to CeO_2 (1 1 1) lattice planes. The EDX analyses to a greater extent corroborated well with the stoichiometry of the sample. However, in certain areas dispersed ceria phase was completely absent, which indicate the influence of high temperature treatment on the surface

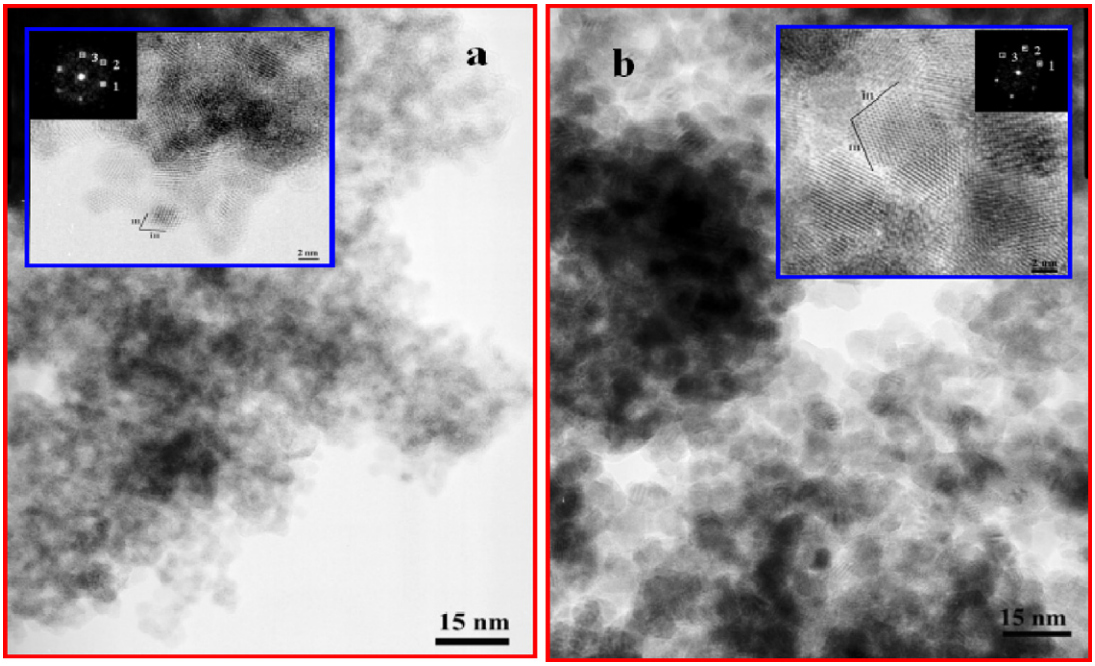

Fig. 5. TEM image of CeO_2/SiO_2 (CS) sample calcined at (a) 773 K (inset: HREM image and DDP pattern) and (b) 1073 K (inset: HREM image and DDP pattern).

segregation of the ceria nanoparticles. The TEM global pictures of the CZS sample calcined at 773 and 1073 K along with their corresponding selected area diffraction patterns (SAED) are shown in Fig. 6a and b, respectively. Here, the existence of small crystals (~5 nm) dispersed over an amorphous matrix with different lighter contrasts is noted. In both the cases the broadening of the rings in the electron diffraction patterns account for the presence of small randomly oriented mixed oxide particles. The position of these reflections, as in the case of unsupported samples, points out the existence of almost exclusively cubic structure. The insets of Figs. 6a and b show HREM images of the CZS sample subjected to 773 and 1073 K, respectively. Well-dispersed very small $Ce_xZr_{1-x}O_2$ particles over the surface of the amorphous silica are mainly observed. Even after 1073 K calcination treatment, there was no significant increase in the size of the particles. Lattice fringes of around 3 Å are extensively observed on very small well-dispersed particles supported on the amorphous contrast of silica. Thus the combined XRD, Raman, XPS and HREM studies provide valuable information on the structural evolution of silica-supported CeO_2 and $Ce_xZr_{1-x}O_2$ mixed oxide catalysts.

The oxygen storage capacity of 773 and 1073 K calcined CS and CZS samples were evaluated by a thermogravimetry method. The percentage weight loss and the corresponding OSC values in terms of μmoles of O_2/g of ceria for both series of samples calcined at 773 and 1073 K are presented in Table 1. As can be noted from Table 1,

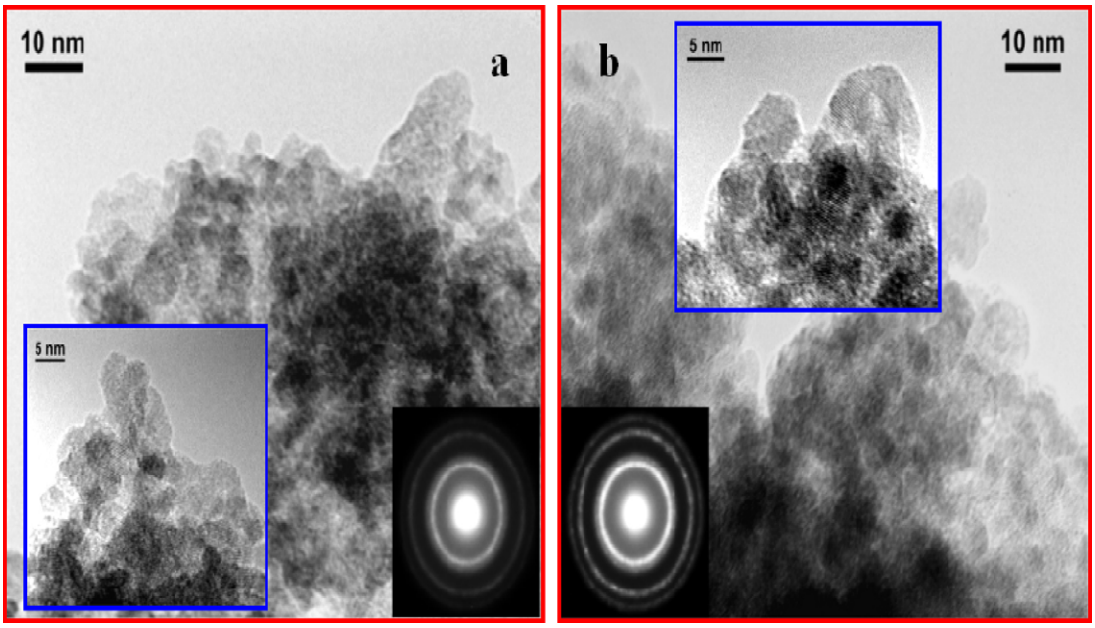

Fig. 6. TEM image of CeO_2–ZrO_2/SiO_2 (CZS) sample calcined at (a) 773 K (inset: HREM image and SAED pattern) and (b) 1073 K (inset: HREM image and SAED pattern).

there is a substantial enhancement in the OSC of CS sample when incorporated with Zr in the ceria lattice. These results clearly establish that highly dispersed and stable CeO_2 or $Ce_xZr_{1-x}O_2$ nano-oxides are responsible for the enhancement in the OSC of the samples. As stated in the experimental section, during the first step of OSC measurement, the sample was heated up to 1073 K. Therefore, it is expected that the OSC values for both 773 and 1073 K calcined samples should be same. However, a small difference in the OSC values is noticed in the case of 1073 K calcined samples as shown in Table 1. This may be due to a decrease in the specific surface area of the samples which were already calcined first at 1073 K. It should be kept in mind that the method adopted for OSC measurements is very sensitive to the nature of the sample. The catalytic properties of these highly dispersed nanocomposite oxides were found to be highly promising for CO oxidation reaction [36]. The CO oxidation is one of the most important reactions in auto exhaust purification three-way catalysis where ceria and ceria-based catalysts are employed as OSC materials. The CO oxidation depends on the OSC property of the ceria-based materials. Thus, high OSC values pertaining to these catalyst systems make them attracting for various other applications.

4. Conclusions

The following conclusions can be drawn from the present investigation. (i) Thermally stable, high surface area nanocrystalline ceria and solid solutions of ceria–zirconia over silica support (colloidal) could be synthesized by a soft chemical route. (ii) The XRD measurements indicated the presence of cubic CeO_2 phase in the case of CS sample. While CZS sample discloses $Ce_{0.75}Zr_{0.25}O_2$ phase at 773 K, and $Ce_{0.6}Zr_{0.4}O_2$ and $Ce_{0.5}Zr_{0.5}O_2$ phases at 1073 K, respectively. This reveals more incorporation of zirconium into the ceria lattice at higher calcination temperature. There is no indication of compound formation between silica and cerium and zirconium oxides. (iii) In line with XRD results, Raman measurements show that silica is not forming any compound with cerium and zirconium oxides. Further, Raman studies suggest the generation of lattice defects and thereby oxygen vacancy formation in the ceria cubic lattice, which are more prominent in the case of Ce–Zr oxides. (iv) XPS measurements indicate the presence of cerium in both 4+ and 3+ oxidation states. At high calcination temperature an increase in the surface content of Ce^{3+} is noted. (v) TEM-HREM results indicate a well-dispersed nano-sized Ce–Zr oxide ($\sim$5 nm) over the surface of amorphous silica. No significant increase in the crystallite size is noted with increase of calcination temperature from 773 to 1073 K. This clearly establishes the significance of the support and the preparation method adopted. (vi) As expected, CZS exhibited high OSC in comparison to CS sample indicating its significance in catalytic applications.

Acknowledgements

P.S. and P.B. thank CSIR, New Delhi for senior research fellowships and L.K. and G.T. thank CSIR, New Delhi for junior research fellowships. Financial support received from Department of Science and Technology, New Delhi, under SERC Scheme (SR/S1/PC-31/2004) is gratefully acknowledged.

References

[1] R.D. Monte, J. Kasper, J. Mater. Chem. 15 (2005) 633.
[2] S. Bernal, J. Kasper, A. Trovarelli, Catal. Today 50 (1999) 173.
[3] B.M. Reddy, P. Bharali, P. Saikia, A. Khan, S. Loridant, M. Muhler, W. Grünert, J. Phys. Chem. C 111 (2007) 1878.
[4] J.R.G. Velasco, J.A. Botas, J.A.G. Marcos, M.A.G. Ortiz, Appl. Catal. B: Environ. 12 (1997) 61.
[5] W.P.A. Jansen, J.M.A. Harmsen, A.W.V.D. Denier, V.D. Gon, J.H.B.J. Hoebink, J.C. Schouten, H.H. Brongersma, J. Catal. 204 (2001) 420.
[6] S. Damyanova, C.A. Perez, M. Schmal, J.M.C. Bueno, Appl. Catal. A: Gen. 234 (2002) 271.
[7] E. Odier, Y. Schuurman, C. Mirodatos, Catal. Today 127 (2007) 230.
[8] S. Wang, G.Q. Lu, Appl. Catal. B: Environ. 19 (1998) 267.
[9] K. Otsuka, M. Hatano, A. Morikawa, J. Catal. 79 (1983) 493.
[10] B.M. Reddy, P. Lakshmanan, A. Khan, S. Loridant, C. Lopez-Cartes, T.C. Rojas, A. Fernandez, J. Phys. Chem. B 109 (2005) 13545.
[11] G.S. Zafiris, R.J. Gorte, J. Catal. 139 (1993) 561.
[12] A. Piras, A. Trovarelli, G. Dolcetti, Appl. Catal. B: Environ. 28 (2000) L77.
[13] M.C.J. Bradford, M.A. Vannice, Catal. Today 50 (1999) 47.
[14] M.J. Tiernan, O.E. Finlayson, Appl. Catal. B: Environ. 19 (1998) 23.
[15] A. Holmgren, B. Andersson, D. Duprez, Appl. Catal. B: Environ. 22 (1999) 215.
[16] A. Trovarelli, Catal. Rev. Sci. Eng. 38 (1996) 439.
[17] H.P. Klug, L.E. Alexander, X-ray Diffraction Procedures for Polycrystalline and Amorphous Materials, 2nd ed., John Wiley and Sons, New York, 1974.
[18] C. Bozo, F. Gaillard, N. Guilhaume, Appl. Catal. A: Gen. 220 (2001) 69.
[19] Practical surface analysis, D. Briggs, M.P. Seah (Eds.), 2nd ed., Auger and X-ray Photoelectron Spectroscopy, vol. 1, Wiley, New York, 1990.
[20] C.D. Wagner, W.M. Riggs, L.E. Davis, J.F. Moulder, in: G.E. Muilenberg (Ed.), Handbook of X-ray Photoelectron Spectroscopy, Perkin-Elmer Corporation, Minnesota, 1978.
[21] B.M. Reddy, A. Khan, Catal. Surv. Asia 9 (2005) 155.
[22] E. Rocchini, A. Trovarelli, J. Llorca, G.W. Graham, W.H. Weber, M. Maciejewski, A. Baiker, J. Catal. 194 (2000) 461.
[23] X.-M. Lin, L.-P. Li, G.-S. Li, W.-H. Su, Mater. Chem. Phys. 69 (2001) 236.
[24] I.E. Wachs, F.D. Hardcastle, S.S. Chan, Spectroscopy 1 (1986) 30.
[25] J.E. Spanier, R.D. Robinson, F. Zhang, S.-W. Chan, I.P. Herman, Phys. Rev. B 64 (2001) 245407.
[26] J.R. McBride, K.C. Hass, B.D. Poindexter, W.H. Weber, J. Appl. Phys. 76 (1994) 2435.
[27] M. Yashima, H. Arashi, M. Kakihana, M. Yoshimura, J. Am. Ceram. Soc. 7 (1994) 1067.
[28] B.M. Reddy, A. Khan, Y. Yamada, T. Kobayashi, S. Loridant, J.C. Volta, Langmuir 19 (2003) 3025.
[29] B.M. Reddy, A. Khan, Y. Yamada, T. Kobayashi, S. Loridant, J.C. Volta, J. Phys. Chem. B 107 (2003) 11475.
[30] I.E. Wachs, G. Deo, J. Phys. Chem. 95 (1991) 5889.
[31] A. Bensalem, F.B. Verduraz, M. Delamar, G. Bugli, Appl. Catal. A: Gen. 121 (1995) 81.
[32] B.M. Reddy, P. Lakshmanan, P. Bharali, P. Saikia, J. Mol. Catal. A: Chem. 258 (2006) 355.
[33] A. Galtayries, M. Crucifix, G. Blanchard, G. Terwagne, R. Sporken, Appl. Surf. Sci. 142 (1999) 159.
[34] H. Behner, J. Wecker, T. Mathee, K. Samwer, Surf. Interf. Anal. 18 (1992) 685.
[35] L. Lepinski, M. Wolcyrz, M. Marchewka, J. Solid State Chem. 168 (2002) 110.
[36] B.M. Reddy, P. Lakshmanan, P. Bharali, P. Saikia, G. Thrimurthulu, M. Muhler, W. Grünert, J. Phys. Chem. C 111 (2007) 10478.